



RESEARCH ARTICLE

10.1029/2019JF005032

Sensitivity of Tidal Bar Wavelength to Channel Width

T. M. Hepkema¹ , H. E. de Swart¹ , and H. M. Schuttelaars² ¹Institute for Marine and Atmospheric Research Utrecht, Utrecht University, Utrecht, The Netherlands, ²Delft Institute of Applied Mathematics, Delft University of Technology, Delft, The Netherlands

Key Points:

- Horizontal eddy diffusivity explains sensitivity of tidal bar wavelength to channel width
- Horizontal eddy diffusivity results in significant additional bed slope effect
- Tidal bar wavelength is expressed in terms of tidal excursion length, friction length scale, and channel width

Correspondence to:

T. M. Hepkema,
t.m.hepkema@uu.nl

Citation:

Hepkema, T. M., de Swart, H. E., & Schuttelaars, H. M. (2019). Sensitivity of tidal bar wavelength to channel width. *Journal of Geophysical Research: Earth Surface*, 124, 2417–2436. <https://doi.org/10.1029/2019JF005032>

Received 5 FEB 2019

Accepted 11 SEP 2019

Accepted article online 14 SEP 2019

Published online 28 OCT 2019

Corrected 7 NOV 2019

This article was corrected on 7 NOV 2019. See the end of the full text for details.

Abstract Tidal bars are repetitive estuarine bedforms with heights of several meters and wavelengths in the order 1–15 km. Understanding their formation and sensitivity to changes in channel characteristics is important as they hamper marine traffic and play a crucial role in the local ecosystem. Recent observations suggest that the local width of the channel is dominant in determining the tidal bar wavelength. However, theoretical studies could not reproduce the sensitivity of the tidal bar wavelength to channel width. This discrepancy between theory and observations suggests that a mechanism is missing. In this study, one of the theoretical models is extended and results in tidal bar wavelengths, lateral mode numbers, and growth rates that agree fairly well with those of natural tidal bars, including the wavelengths dependency on estuary width. An important extension of the model concerns the bed slope induced diffusive suspended load transport of sediments. With this, it is explained why previously, the modelled tidal bar wavelengths depend only weakly on estuary width and why in the extended model it does. This has, from a modelling point of view, general implications for morphological models using a total load sediment transport formulation with a so-called bed slope parameter.

1. Introduction

Many tidal channels have a rhythmic bottom topography consisting of so-called tidal bars. Examples are the Ord River estuary in Australia, the Exe estuary in England, the Netarts bay in the United States, and the Western Scheldt in the Netherlands (see Figure 1 and Leuven et al., 2016 for many more examples). These bars have wavelengths of 1–15 km and heights of several meters. As tidal bars hamper marine traffic and provide rich feeding grounds for many living organisms, it is important to understand their formation and sensitivity to tidal channel characteristics (i.e., channel width, depth, and currents). These characteristics may change due to, for example, dredging, sea level rise, or land reclamation. The sensitivity of the tidal bars to changes in channel characteristics was previously investigated by measurements, laboratory experiments, idealized models, and complex numerical models.

By analyzing data of 25 tidal bars in creeks in South Carolina and in the Salmon River estuary, Dalrymple and Rhodes (1995) found that the tidal bar wavelength is typically six times the channel width. Also, Leuven et al. (2016) found that the tidal bar wavelength correlates the strongest with channel width, compared to other channel characteristics such as depth and current velocity. They came to this conclusion by measuring the wavelength of 190 tidal bars in Google Earth. Furthermore, Tambroni et al. (2005) investigated morphodynamic equilibria in tidal channels and inlets in a laboratory. Their tidal bars formed after 50 tidal cycles with wavelengths of approximately three times the channel width.

To gain fundamental understanding about tidal bars, Seminara and Tubino (2001) analyzed a 3D-idealized model. In their model, the section of the channel, in which the tidal bars are studied, is assumed to be short with respect to the tidal wavelength, width variations, and depth variations. This setting differs from, for example, Schuttelaars and de Swart (1999) and ter Brake and Schuttelaars (2011), where the formation of tidal bars in a short semienclosed channel was investigated. Seminara and Tubino (2001) demonstrated that tidal bars can form as a free instability of an equilibrium state that describes a horizontally uniform tidal current over a horizontal bed. They found that the wavelengths of their modelled bars are comparable with those of observed bars. It further follows from their results that the ratio of channel width over wavelength of the bars scales close to linearly with the width-to-depth ratio. This implies that for a constant depth, the wavelength hardly depends on channel width. Schramkowski et al. (2002) showed that a depth-averaged model is able to model characteristics of tidal bars and that a 3D model is not needed. They included the

©2019. The Authors.

This is an open access article under the terms of the Creative Commons Attribution License, which permits use, distribution and reproduction in any medium, provided the original work is properly cited.

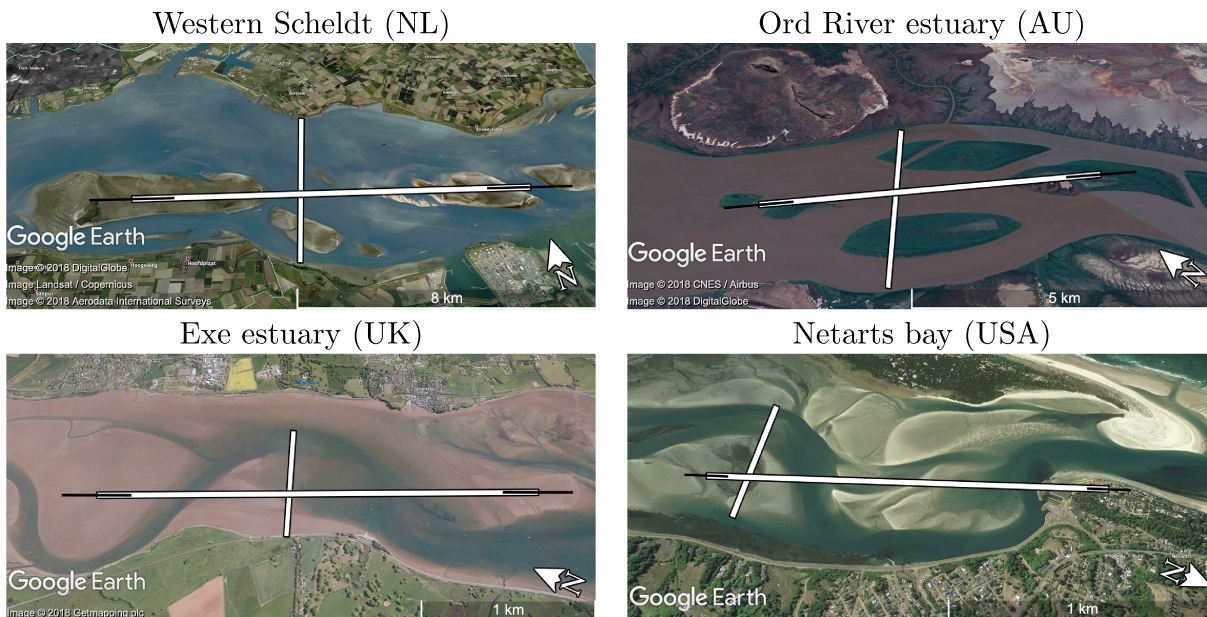


Figure 1. Measured tidal bar wavelength and channel width of four tidal channels in Google Earth.

local inertia terms in the momentum balance and showed that the current velocity and the water depth are also important in determining the tidal bar wavelength. This model also yields a tidal bar wavelength that only depends weakly on channel width (Leuven et al., 2016). Garotta et al. (2006) confirmed that a 2D model is sufficient and moreover showed that forcing by a tidal current that is either ebb or flood dominant leads to a net migration of bars.

Thus, the idealized models are not able to reproduce the observed sensitivity of tidal bar length on channel width. This could be a consequence of the many assumptions made in these models. To clarify this, numerical models, which contain less constraints, are helpful. Such a study was carried out by Hibma et al. (2004). Their numerical experiments were designed such that comparison with the idealized studies was possible. They found tidal bar wavelengths that are comparable with those found by Schramkowski et al. (2002). However, despite expectations after the work of Schramkowski et al. (2002), the wavelength was, besides sensitive to current velocity and channel depth, also sensitive to channel width. Yet they did not investigate this further. Also, van der Wegen and Roelvink (2008) found that the wavelength depends on both the estuary width, depth, and the current velocity. In addition, van de Lageweg and Feldman (2018) found that, in a strongly convergent estuary, an increase in basin width results in longer bars.

The considerations above show in particular that the idealized models are not able to explain the observed (and numerically reproduced) dependence of tidal bar length on channel width. A likely explanation for this discrepancy is that one or more essential physical processes are missing in these models. Compared with numerical model formulations, it turns out that the idealized models do not account for the effects of turbulent exchange of momentum and sediment in the horizontal plane. The intensities of these processes are measured by a horizontal eddy viscosity coefficient and a horizontal eddy diffusion coefficient, respectively. Therefore, in the present study, the model of Schramkowski et al. (2002) is extended with terms that describe horizontal turbulent exchange processes. Moreover, a critical current velocity for sediment erosion is added to achieve consistency with all other models.

The first aim of this work is to show that the extended model can mimic the pattern of observed tidal bars. The second aim is to show that the model can reproduce the sensitivity of tidal bar wavelength to channel width. The first and second aim are treated in section 3. Finally, we aim at explaining why the incorporation of the new processes results in a dependence of the tidal bar wavelength to channel width (section 4).

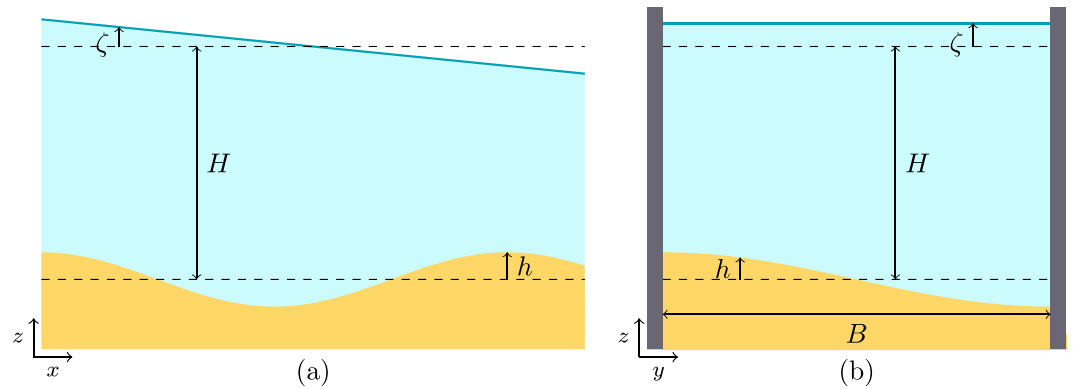


Figure 2. (a) Along-channel section in (x, z) -plane. (b) Cross-channel section in (y, z) -plane. H denotes the undisturbed depth, ζ the free surface elevation, h the bottom height, and B the channel width. The arrows with x , y , and z denote the direction of the spatial coordinates.

2. Model and Method

2.1. Governing Equations

The formation of tidal bars is modelled in a section of a tidal channel which is short compared to both the tidal wavelength and the e -folding length scale of channel width convergence. The model domain under consideration therefore consists of a 2D rectangular channel of fixed width B , mean depth H , and infinite length (Figure 2). Note that by channel width B , the total width of the channel is meant (see also Figure 1). The hydrodynamics is modelled by the depth-averaged shallow water equations including horizontal eddy viscosity and assuming the rigid-lid approximation. The latter constitutes to only retaining the free surface elevation in the pressure gradient. Coriolis effects are not considered, and the bed shear stress and internal stresses are linearized. The depth-integrated sediment concentration is modelled by an advection-diffusion equation based on ter Brake and Schuttelaars (2010) and extended by including a critical velocity for erosion. The bed evolution (Exner) equation follows from the conservation of sediment mass. Since the convergence of sediment transport is almost periodic (with a period equal to the principal tidal constituent), the subtidal convergence is small compared to the instantaneous convergence of sediment transport. Therefore, the patterns evolve on a much larger time scale than the tidal period and is determined by the tidally averaged convergence of sediment transport (see Krol, 1991 for a discussion on the errors introduced by this approximation). The differences with the model of Schramkowski et al. (2002) are the critical velocity for erosion, the horizontal eddy viscosity, and horizontal eddy diffusivity. The resulting governing equations read

$$\nabla \cdot ((H - h)\mathbf{u}) = 0, \quad (1)$$

$$\frac{\partial \mathbf{u}}{\partial t} + (\mathbf{u} \cdot \nabla)\mathbf{u} + \frac{r\mathbf{u}}{H - h} - \nu \nabla^2 \mathbf{u} = \mathbf{F}_p, \quad (2)$$

$$\frac{\partial C}{\partial t} + \nabla \cdot (\mathbf{u}C) - \nabla \cdot \left(\mu \nabla C + \mu \frac{w_s}{\kappa_v} \beta_b C \nabla h \right) = E - D, \quad (3)$$

$$(1 - \hat{p}) \frac{\partial h}{\partial t} + \nabla \cdot \langle \mathbf{q}_s + \mathbf{q}_b \rangle = 0. \quad (4)$$

The space and time coordinates are $\mathbf{x} = (x, y)$ [m] and t [s], respectively. Furthermore, $\mathbf{u}(t, \mathbf{x}) = (u, v)$ [m s^{-1}] is the depth-averaged flow velocity vector, $C(t, \mathbf{x})$ [$\text{m}^3 \text{m}^{-2}$] the depth-integrated volumetric sediment concentration, and $h(t, \mathbf{x})$ [m] the height of the bottom with respect to a flat undisturbed bottom (see Figure 2). H [m] is the undisturbed water depth, r [m s^{-1}] a friction coefficient, and ν [$\text{m}^2 \text{s}^{-1}$] the horizontal eddy viscosity coefficient. Moreover, μ [$\text{m}^2 \text{s}^{-1}$] is the horizontal eddy diffusion coefficient, w_s [m s^{-1}] the sediment settling velocity, κ_v [$\text{m}^2 \text{s}^{-1}$] the vertical eddy diffusivity coefficient, β_b a deposition parameter, and \hat{p} the porosity parameter. The prescribed pressure gradient force per mass unit $\mathbf{F}_p = -g \nabla \zeta$ [m s^{-2}], with g [m s^{-2}]

the gravitational acceleration and $\zeta(t, \mathbf{x})$ [m] the free surface elevation, drives a tidal current in the channel of which the dominant constituent has radian frequency σ [s⁻¹] and a typical amplitude U . Furthermore, $\langle \cdot \rangle$ is the average over one tidal cycle with period $2\pi/\sigma$. Erosion E and deposition D are defined as

$$E = \alpha \mathcal{H} (\|\mathbf{u}\|^2 - u_c^2) (\|\mathbf{u}\|^2 - u_c^2) \quad \text{and} \quad D = \gamma C,$$

with \mathcal{H} the Heaviside function, which is zero (one) when its argument is (not) negative and $\|\cdot\|$ denotes the Euclidean norm of a vector. In these expressions, α [s m⁻¹] is an erosion parameter, u_c [m s⁻¹] the critical velocity for erosion, and γ [s⁻¹] a deposition parameter. Lastly, q_s [m² s⁻¹] is the transport of suspended sediment and q_b [m² s⁻¹] the transport of sediment as bed load. In Schramkowski et al. (2002), it is argued that the bed load transport is much smaller than the suspended load transport but that the bed slope contribution to the bed load transport should be maintained. Here the suspended load transport is extended by a diffusivity term based on ter Brake and Schuttelaars (2010). The sediment transport formulations read

$$\mathbf{q}_s = \mathbf{u}C - \mu \left(\nabla C + \frac{w_s}{\kappa_v} \beta_b C \nabla h \right) \quad \text{and} \quad \mathbf{q}_b = -\hat{s} \kappa_* \|\mathbf{u}\|^3 \nabla h,$$

where \hat{s} [s² m⁻¹] is a bed load transport constant and κ_* a bed slope parameter.

The bottom friction coefficient $r = 8/(3\pi)c_d \mathcal{U}$ is chosen to scale with a typical current velocity amplitude. The horizontal eddy diffusivity coefficients $\nu = c_h^u \mathcal{U} B$ and $\mu = c_h^c \mathcal{U} B$ scale with current velocity and the channel width. The vertical eddy diffusivity $\kappa_v = c_v \mathcal{U} H$ scales with current velocity and the undisturbed channel depth. Here c_h^c , c_h^u , c_v are constants and \mathcal{U} is a typically velocity, which will be specified in the next section. All parameters are summarized in Table 1. The bed load transport formulation and constants \hat{s} and κ_* are taken from Schramkowski et al. (2002) and based on Bailard (1981). The value of the erosion parameter α is also taken from Schramkowski et al. (2002) and based on Smith and McLean (1977), the deposition parameters γ and β_b are based on the derivation in ter Brake and Schuttelaars (2010), and the settling velocity w_s corresponds to sediment with a median grain diameter $d_{50} = 0.15$ mm. For the reasoning behind the values of the sediment parameters, we refer to the books of Dyer (1986) and Soulsby (1997).

The lateral boundary conditions imposed are

$$v = 0, \quad \frac{\partial C}{\partial y} = 0, \quad \frac{\partial h}{\partial y} = 0 \quad \text{and} \quad \frac{\partial u}{\partial y} = 0 \quad \text{at} \quad y = 0, B. \quad (5)$$

This means that there is neither transport of water nor sediment through the solid boundaries of the channel. Furthermore, all variables are assumed periodic in the longitudinal direction. Further details and underlying assumptions of the model are given in Schramkowski et al. (2002).

2.2. Linear Stability Analysis

Similar to the system in Schramkowski et al. (2002), the system (1)–(5) admits a spatially uniform equilibrium solution $((\mathbf{F}_p)_{\text{eq}}, \mathbf{u}_{\text{eq}}, C_{\text{eq}}, h_{\text{eq}})$, which is here chosen to be an M_2 tidal flow

$$\mathbf{u}_{\text{eq}} = (u_{\text{eq}}, v_{\text{eq}}) = (U \cos(\sigma t), 0)$$

over a flat bottom $h_{\text{eq}} = 0$, with U [m s⁻¹] the constant amplitude of the longitudinal equilibrium velocity u_{eq} . The corresponding pressure gradient $(\mathbf{F}_p)_{\text{eq}} = -g \nabla \zeta_{\text{eq}}$ and sediment concentration C_{eq} are given in Appendix A. The typical current velocity scale \mathcal{U} is chosen to be the amplitude of the equilibrium velocity U . Other harmonic compositions can be added to u_{eq} , but are not considered here.

Tidal bars form as an instability on this spatially uniform equilibrium, $((\mathbf{F}_p)_{\text{eq}}, \mathbf{u}_{\text{eq}}, C_{\text{eq}}, h_{\text{eq}})$. Perturbations in the bottom $h_{\text{eq}} + h'$ result in perturbations in the flow $\mathbf{u}_{\text{eq}} + \mathbf{u}'$, the pressure gradient $-g(\nabla \zeta_{\text{eq}} + \nabla \zeta')$, and the sediment concentration $C_{\text{eq}} + C'$. These perturbations, in turn, result in positive or negative feedbacks resulting in growth or decay of the bottom perturbations h' . The pattern with the largest growth overtakes the others and yields the length and time scale of the pattern that is formed initially (Dodd et al., 2003).

Substituting $\zeta = \zeta_{\text{eq}} + \zeta'$, $u = u_{\text{eq}} + u'$, $v = v_{\text{eq}} + v'$, $C = C_{\text{eq}} + C'$, and $h = h_{\text{eq}} + h'$, in equations (1)–(4) and linearizing the resulting equations, yields a system of linear partial differential equations in the primed variables, which are perturbations on the equilibrium variables. The linearized equations are given in Appendix

Table 1
Parameters and Their Value (Range) After ter Brake and Schuttelaars (2010) and Schramkowski et al. (2002)

Parameter	Value(s)	Units	Name
H	1.2 – 10	m	Undisturbed water depth
B	800 – 7000	m	Channel width
U	0.6 – 1	m s^{-1}	Amplitude equilibrium velocity
$r = \frac{8}{3\pi} c_d \mathcal{U}$		m s^{-1}	Friction coefficient
$\kappa_v = c_v \mathcal{U} H$		$\text{m}^2 \text{s}^{-1}$	Vertical eddy diffusivity coefficient
$\nu = c_h^\mu \mathcal{U} B$		$\text{m}^2 \text{s}^{-1}$	Horizontal eddy viscosity coefficient
$\mu = c_h^c \mathcal{U} B$		$\text{m}^2 \text{s}^{-1}$	Horizontal eddy diffusion coefficient
$\mathcal{U} = U$		m s^{-1}	Typical current velocity
$\gamma = \frac{w_s^2}{\kappa_v} \beta_b$		s^{-1}	Deposition parameter
$\Lambda = \kappa_* \hat{s} \langle u_{eq}^3 \rangle$		$\text{m}^2 \text{s}^{-1}$	Bed load bed slope parameter
$\beta_b = \left(1 - e^{-\frac{w_s}{\kappa_*} H}\right)^{-1}$			Deposition parameter
g	9.81	m s^{-2}	Gravitational acceleration
σ	$1.4 \cdot 10^{-4}$	s^{-1}	M_2 tidal frequency
w_s	0.013	m s^{-1}	Settling velocity
α	$5 \cdot 10^{-6}$	s m^{-1}	Erosion parameter
u_c	0 – 0.3	m s^{-1}	Critical depth-averaged velocity for erosion
\hat{s}	$3 \cdot 10^{-4}$	$\text{s}^2 \text{m}^{-1}$	Bed load transport constant
\hat{p}	0.4		Porosity parameter
c_d	0.0025		Drag coefficient
κ_*	2		Bed load bed slope parameter
c_v	0.001		Vertical diffusivity constant
c_h^c	0 – 0.0035		Horizontal diffusivity constant
c_h^μ	0 – 0.001		Horizontal viscosity constant

B. This system of equations, together with the boundary conditions (5) in terms of the primed variables, allow for solutions, which are linear combinations of

$$\begin{pmatrix} \zeta' \\ u' \\ v' \\ C' \\ h' \end{pmatrix} = \text{Re} \left\{ \begin{pmatrix} \hat{\zeta}(t) \cos(l_n y) \\ \hat{u}(t) \cos(l_n y) \\ \hat{v}(t) \sin(l_n y) \\ \hat{C}(t) \cos(l_n y) \\ \hat{h}(t) \cos(l_n y) \end{pmatrix} e^{ikx} \right\}, \quad (6)$$

for every natural number n and real number $k > 0$. Here $l_n = n\pi/B$ and $\hat{\zeta}$, \hat{u} , \hat{v} , \hat{C} , and \hat{h} are complex valued functions of time. The number n is henceforth referred to as the mode number and is related to the number of bars and troughs in the lateral direction of the channel. For example, a pattern with mode number $n = 1$ corresponds to an alternating bar pattern and the pattern with $n = 2$ has one bar or a trough in the middle of the channel.

Since the perturbations in the bottom vary on a time scale that is much longer than the time scale on which perturbations of the other variables vary, the bottom is assumed to be constant during one tidal cycle. That is, \hat{h} only depends on a long morphodynamic time scale while $\hat{\zeta}$, \hat{u} , \hat{v} , and \hat{C} depend on the short hydrodynamical time scale. This allows for calculating the fast variables $\hat{\zeta}$, \hat{u} , \hat{v} , and \hat{C} , assuming a fixed bottom. The so-called “flow over topography problem” is solved during one tidal cycle.

Substituting equation (6) in the linearized continuity, momentum, and concentration equation for a constant \hat{h} results in a system of ordinary differential equations for $\hat{\zeta}$, \hat{u} , \hat{v} , and \hat{C} . The solution to this system of equations is approximated by a truncated Fourier series. This Fourier series contains the residual component and overtides with frequencies $p\sigma$, with p an integer. Because the equations are linear and inhomogeneous,

the resulting $\hat{\zeta}$, \hat{u} , \hat{v} , and \hat{C} will be linear in the amplitude of the bed perturbations \hat{h} . Taking this into account, the amplitudes are approximated by choosing a large enough natural number N and substituting

$$(\hat{\zeta}, \hat{u}, \hat{v}, \hat{C}) = \hat{h} \sum_{p=-N}^N (\tilde{\zeta}_p, \tilde{u}_p, \tilde{v}_p, \tilde{C}_p) e^{ip\sigma t} \quad (7)$$

in the ordinary differential equations. Here $\tilde{\zeta}_p$, \tilde{u}_p , \tilde{v}_p , and \tilde{C}_p for $p = -N, \dots, N$ are complex amplitudes, independent of \hat{h} . This results in a system of $4(2N+1)$ algebraic equations in $\tilde{\zeta}_p$, \tilde{u}_p , \tilde{v}_p , and \tilde{C}_p , which can be solved numerically. Recall that, since the resulting velocity and concentration field is solved for a fixed h' , the coefficients $\tilde{\zeta}_p$, \tilde{u}_p , \tilde{v}_p , and \tilde{C}_p depend on n and k . That is to say, the obtained (ζ', u, v, C) describe how the flow, the pressure gradient, and the concentration react to the bottom perturbations $h' = \text{Re} \left\{ \hat{h} \cos(l_n y) e^{ikx} \right\}$.

The next step is to determine the bed evolution. The linearized Exner equation reads

$$(1 - \hat{p}) \frac{\partial h'}{\partial t} + \nabla \cdot \langle \mathbf{q}'_s + \mathbf{q}'_b \rangle = 0, \quad (8)$$

with

$$\mathbf{q}'_s = \mathbf{u}' C_{\text{eq}} + \mathbf{u}_{\text{eq}} C' - \mu \left(\nabla C' + \frac{w_s}{\kappa_v} \beta_b C_{\text{eq}} \nabla h' \right) \quad \text{and} \quad \mathbf{q}'_b = -\Lambda \nabla h', \quad (9)$$

where $\Lambda = \hat{\delta} \kappa_* \langle |u_{\text{eq}}^3| \rangle$. Since ζ' , u , v , and C are explicitly calculated in terms of h' , substituting these expressions in equation (8) results in a single equation for h' and hence for \hat{h} ,

$$\frac{\partial \hat{h}}{\partial t} = \omega \hat{h}, \quad (10)$$

with complex growth rate

$$\omega = \frac{-1}{1 - \hat{p}} \left(\frac{ikU}{2} (\tilde{C}_1 + \tilde{C}_{-1}) + \mu(k^2 + l_n^2) \tilde{C}_0 + \mu \frac{w_s}{\kappa_v} \beta_b \tilde{C}_{\text{eq},0} (k^2 + l_n^2) + \Lambda(k^2 + l_n^2) \right), \quad (11)$$

in which the variables with the tildes are defined in equation (7) and $\tilde{C}_{\text{eq},0}$ in Appendix A. The real part of the complex growth rate represents the actual growth rate of the bottom perturbation and $-\text{Im}\{\omega\}/k$ its migration speed. Here ω turns out to be real because u_{eq} consists of one tidal constituent.

The preferred wavenumber and mode number k_{pref} and n_{pref} are defined as those for which the growth rate ω is maximal,

$$\omega(k_{\text{pref}}, n_{\text{pref}}) = \max_{k, n} \{ \omega(k, n) \}.$$

The preferred growth rate $\omega_{\text{pref}} = \omega(k_{\text{pref}}, n_{\text{pref}})$ and the preferred wavelength $\lambda_{\text{pref}} = 2\pi/k_{\text{pref}}$ is the wavelength that can be compared to the distance between natural tidal bars. The preferred wavenumber, mode number, and growth rate are found using the optimization method ‘‘Brent’’ (Press et al., 2007).

3. Results

3.1. Verification

The first objective is to verify that the model produces preferred wavelengths λ_{pref} , mode numbers n_{pref} , and e -folding growth time $1/\omega_{\text{pref}}$ that resemble those of bars that are observed in nature. For this, we selected four natural tidal channels. These four are chosen because they differ in width, depth, and current velocities and roughly satisfy the model assumptions. Table 2 summarizes the geometric and current characteristics of these channels, as well as the observed wavelength λ_{pref}^M and mode number n_{pref}^M of the tidal bars. The wavelength, mode number, and channel width are obtained from Google Earth (Figure 1). This is done by identifying the pattern of the form $\cos(n\pi y/B) \cos(kx)$ (as in equation (6)), which represent the observed channels in Google Earth most accurately. The wavelength λ_{pref}^M is measured as the distance between successive crests. The uncertainty in the wavelength results from the uncertainty of the location of the crests of the bars. An alternating bar pattern ($n_{\text{pref}}^M = 1$) represents the patterns in the Exe estuary and the Netarts bay best. The patterns in the Ord and the Western Scheldt are described by patterns with a mode number close to three. The width of the pattern that fits best is as illustrated in Figure 1.

Table 2
Measured Wavelength λ_{pref}^M , Mode Number n_{pref}^M , Width B , Undisturbed Depth H , and M_2 Current Amplitude U

	B [km]	H [m]	U [m s^{-1}]	λ_{pref}^M [km]	n_{pref}^M
Western Scheldt	7.0	10.0	1.0	12.7 ± 2.8	3
Ord River estuary	3.8	4.0	0.6	6.7 ± 1.4	3
Exe estuary	1.0	2.6	0.6	3.1 ± 0.3	1
Netarts bay	0.8	1.2	0.6	1.9 ± 0.2	1

The currents and undisturbed depths of the Western Scheldt, Ord River estuary, Exe estuary, and Netarts bay are based on Cancino and Neves (1999), Wolanski et al. (2001), Herrmann and Hübner (1982), and Glanzmann et al. (1971), respectively. Furthermore, these papers report that the considered channels are vertically well mixed (i.e., small vertical salinity gradients) and the tides predominantly semidiurnal with free surface elevation amplitudes of 1–2 m. The sediment properties are assumed to be similar in all channels (following Leuven et al., 2016). Typical time scales at which these bars evolve are of the order of decades.

The left column of Figure 3 shows the growth curves (i.e., graphs of $\omega(k, n)$) for the four different channels. The red vertical line represents the measured wavenumber and the red area the measurement uncertainty. The right column shows the bottom pattern corresponding to the preferred wavenumber and mode number on which the residual current is shown with arrows. The figure reveals that, using realistic parameter values, the model yields wavelengths of tidal bars that are of the same order of magnitude as those of bars observed in nature. Also, the preferred mode numbers n_{pref} are in the right order of magnitude. They agree for the Exe estuary and the Netarts bay and for the Western Scheldt and the Ord River estuary the difference is one. Note that for the Ord River estuary, the maximal growth rates for the different mode numbers $n = 1$, $n = 2$, and $n = 3$ are similar. Lastly, the e -folding growth time is in the order of decades.

3.2. Sensitivity of Tidal Bar Wavelength to Channel Width

The second objective is to show that the extended model reproduces the sensitivity of the preferred wavelength to channel width. The lower lines in the top panels of Figure 4 (indicated by $c_h^c = 0$) show the relation between the preferred wavelength λ_{pref} and the channel width B for the four channels when the horizontal eddy diffusivity μ , horizontal eddy viscosity ν , and the critical velocity for erosion u_c are all zero. This case corresponds to the original model of Schramkowski et al. (2002), where the preferred wavelength, as Leuven et al. (2016) noted, remains of the same order of magnitude over the whole range of channel widths. Small increases in channel width result in slight increases of the wavelength λ_{pref} . However, when the width B is increased even more, a pattern with a larger mode number n but with a smaller λ_{pref} has the largest growth rate. That is, the preferred mode number jumps to a higher one.

The upper lines in the top panels of Figure 4 show the preferred wavelength versus channel width for the same parameter values, but with a nonzero horizontal eddy diffusivity. They reveal that, for all four channels, when horizontal eddy diffusivity $\mu = c_h^c UB$, is nonzero, the relative change of the preferred wavelength λ_{pref} over the considered range of channel widths is larger than when the horizontal eddy diffusivity is neglected. That is, when $\mu \neq 0$, the preferred wavelength λ_{pref} is more dependent on channel width B than when $\mu = 0$. The jumps in mode number occur later than in the case when horizontal eddy diffusivity is neglected. In fact, the middle (and top) row shows that the preferred mode number n_{pref} decreases when the eddy diffusivity is taken into account. That is, the addition of horizontal eddy diffusivity reduces the growth of patterns with large gradients (high mode numbers and wavenumbers).

The addition of eddy viscosity or a critical velocity of erosion does not strongly alter the relation between the preferred wavelength and channel width. This is shown in Figure 5 for the Western Scheldt case. The right panels show the preferred wavelength versus channel width when eddy viscosity is taken into account. The left panels show the same when the critical velocity for erosion is nonzero. The eddy diffusivity is neglected in the top panels while it is taken into account in the lower panels. The difference between the lines in the top panels is minimal compared to the lower line in the top left panel of Figure 4, where both the eddy viscosity and the critical velocity for erosion are zero.

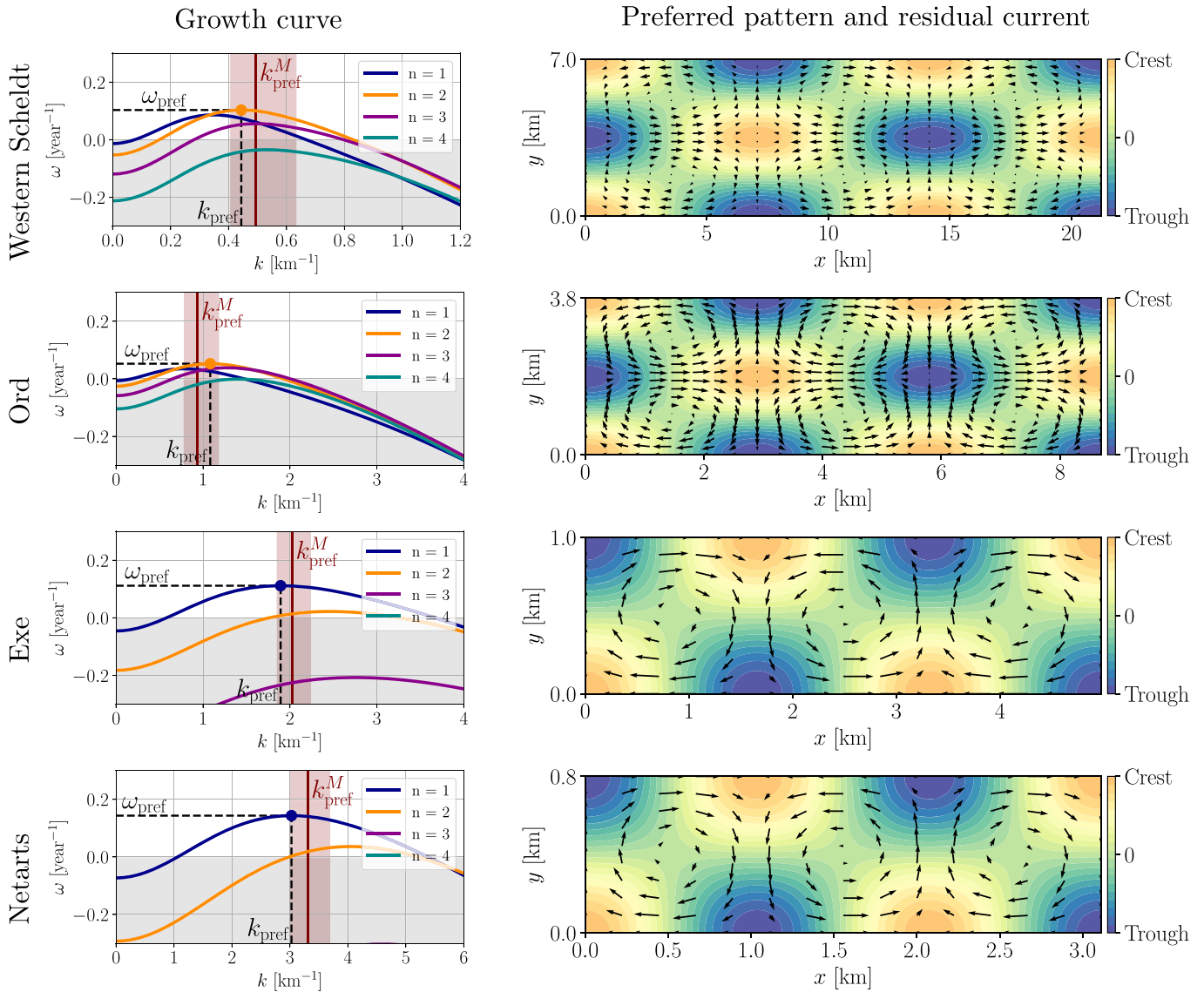


Figure 3. Left: Growth rate ω versus wavenumber k for different mode numbers n and four different channels (rows). The red vertical lines denote the measured wavenumber $k_{\text{pref}}^M = 2\pi/\lambda_{\text{pref}}^M$ as in Table 2 and the red area the measurement uncertainty. Right: The preferred bottom pattern versus space for each channel. The arrows denote the residual current. Parameters are as in Tables 1 and 2 with $c_h^u = c_h^c = 0.001$ and $u_c = 0.3 \text{ m s}^{-1}$.

3.3. Different Contributions to the Growth Rate ω

The third objective is to explain why the incorporation of the horizontal eddy diffusivity results in a dependence of the preferred wavelength λ_{pref} on channel width B . To facilitate the subsequent discussion in which the third objective is met, we analyze the different terms of the growth rate ω in more depth. To simplify expressions, the critical velocity of erosion u_c and the horizontal eddy viscosity ν are henceforth neglected, since in the previous section, it is shown they do not significantly alter the relation between channel width and tidal bar wavelength.

The growth rate consists of four terms,

$$\omega = \frac{-1}{1 - \hat{p}} \left(\underbrace{\frac{ikU}{2} (\tilde{C}_1 + \tilde{C}_{-1})}_{\omega_{\text{adv}}} + \underbrace{\mu(k^2 + l_n^2) \tilde{C}_0}_{\omega_{\text{diff depth-int}}} + \underbrace{\mu \frac{W_s}{\kappa_v} \beta_b \tilde{C}_{\text{eq},0} (k^2 + l_n^2)}_{\omega_{\text{diff bed slope}}} + \underbrace{\Lambda(k^2 + l_n^2)}_{\omega_{\text{bl bed slope}} \right), \quad (12)$$

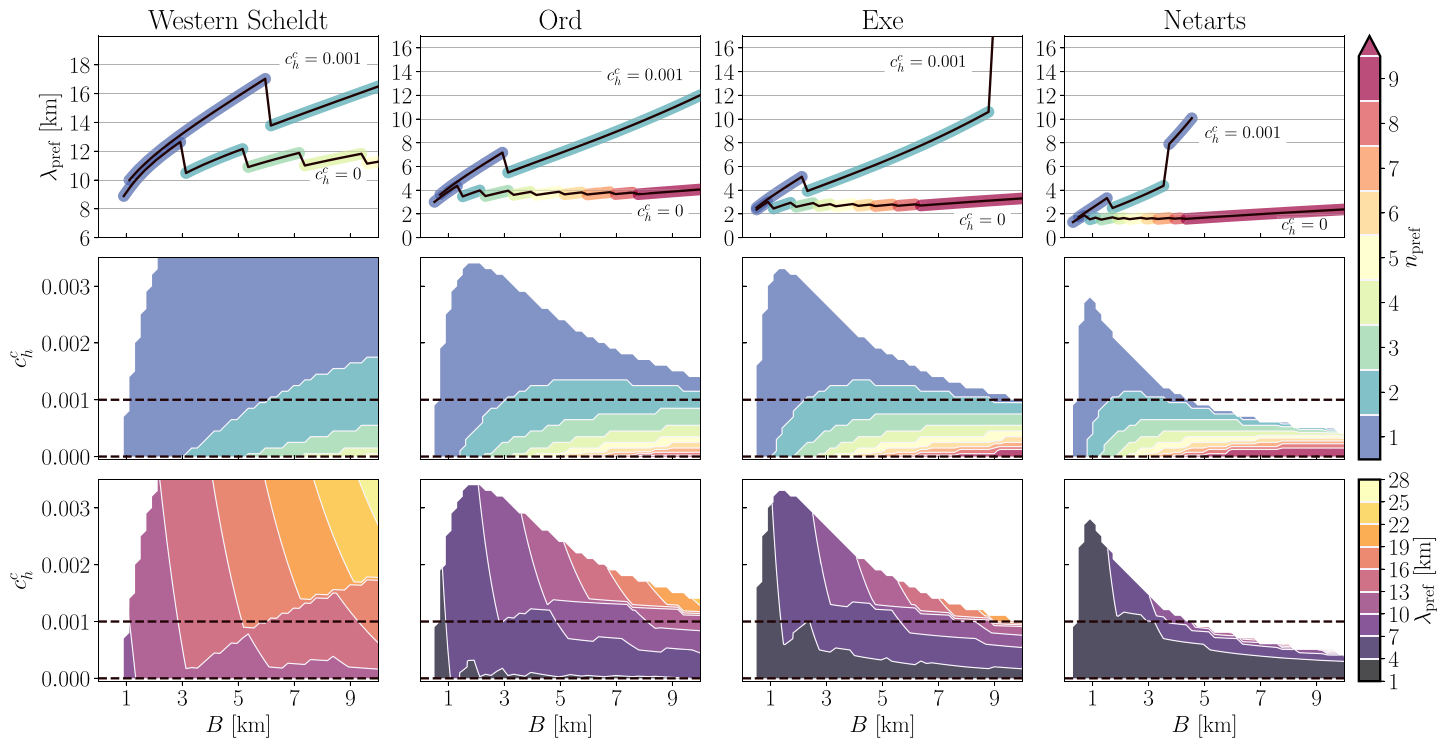


Figure 4. Top row: Preferred bar wavelength λ_{pref} versus channel width B for the four different channels and two values of the eddy diffusivity parameter c_h^c . The colors indicate the preferred mode number n_{pref} . Middle row: Preferred mode number n_{pref} versus channel width B and eddy diffusivity parameter c_h^c for the four different channels. Bottom row: As middle row, but the preferred wavelength λ_{pref} versus channel width B and eddy diffusivity parameter c_h^c . The lines in the top row are two sections of the middle and bottom row (dashed lines). The white areas in the middle and bottom panels denote that for these parameters, there does not exist a pair (k, n) for which $\omega(k, n) > 0$ (no bottom perturbation pattern grows). The parameters are as in Tables 1 and 2 with $c_h^u = 0$ and $u_c = 0 \text{ m s}^{-1}$.

where the factor $-1/(1 - \hat{p})$ is understood to be part of the different terms. The first term, ω_{adv} , results from advective sediment transport. The second and third terms, $\omega_{\text{diff depth-int}}$ and $\omega_{\text{diff bed slope}}$, are due to diffusive sediment transport and the fourth term $\omega_{\text{bl bed slope}}$ originates from the effect of bed slopes on bed load sediment transport. Figure 6 shows the contribution of the different mechanisms to the growth rate versus wavenumber k for parameter values representative for the Western Scheldt. Next, we discuss the physics of the different terms of the growth rate ω .

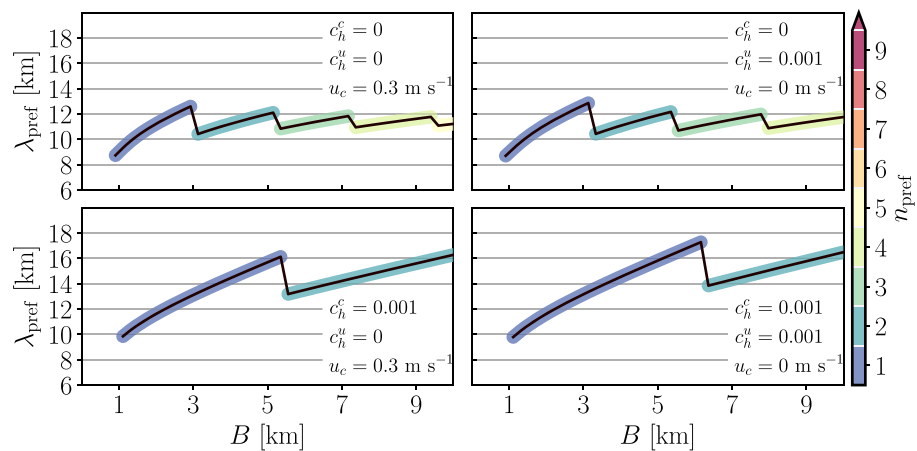


Figure 5. Preferred wavelength λ_{pref} versus channel width B . In the left panels, a critical erosion velocity is included, and in the right panels, eddy viscosity is included. In the top panels, the eddy diffusivity is neglected while the lower panels, it is not. The remaining parameters are as in Tables 1 and 2 for the Western Scheldt.

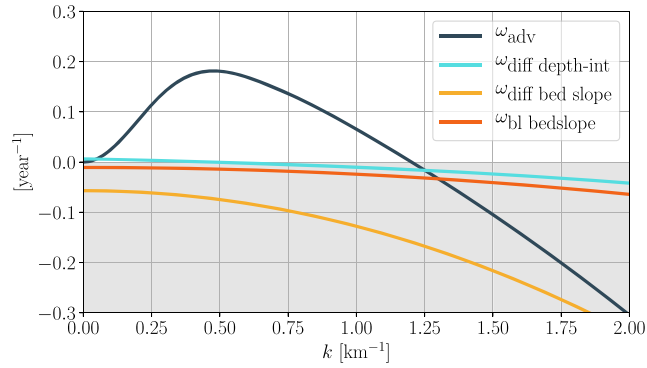


Figure 6. The four different parts of the growth rate ω versus wavenumber k with $n = n_{\text{pref}} = 2$. Parameters are as in Tables 1 and 2 for the Western Scheldt case and $c_h^u = 0$ and $u_c = 0 \text{ m s}^{-1}$.

The first term in equation (12) is the advective part of the growth rate ω_{adv} and relates to convergence of tidally averaged advective sediment transport, that is,

$$-\langle \nabla \cdot (\mathbf{u}' C_{\text{eq}} + \mathbf{u}_{\text{eq}} C') \rangle.$$

To analyze ω_{adv} , consider the p -th Fourier mode of the linearized concentration equation (3) with $u_c = 0$,

$$\underbrace{\text{inertia } ip\sigma\tilde{C}_p}_{\text{erosion } \alpha U(\tilde{u}_{p+1} + \tilde{u}_{p-1})} + \underbrace{\text{advection } \frac{ikU}{2} \left((\tilde{C}_{p+1} + \tilde{C}_{p-1}) + \frac{\tilde{C}_{\text{eq},p+1} + \tilde{C}_{\text{eq},p-1}}{H} \right)}_{\text{deposition } \gamma\tilde{C}_p} + \underbrace{\text{diffusion } \mu(k^2 + l_n^2) \left(\tilde{C}_p + \frac{w_s}{\kappa_v} \beta_b \tilde{C}_{\text{eq},p} \right)}_{\text{diffusion}} = 0. \quad (13)$$

The dominant balance in the M_2 concentration equation for $k \approx k_{\text{pref}}$ is between erosion and deposition in all four considered cases. For the Western Scheldt, this is shown in Figure 7. Then, neglecting the M_4 components in the perturbed current u' (as they are small compared to the M_2 components), the M_2 components of the perturbed concentration reads

$$\tilde{C}_{\pm 1} \approx \frac{\alpha U}{\gamma} \tilde{u}_0. \quad (14)$$

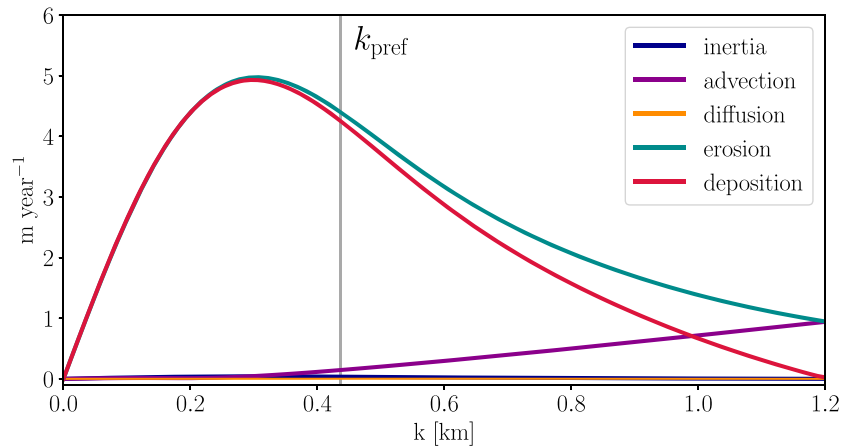


Figure 7. The absolute value of each term in one of the M_2 ($p = 1$) concentration equations (13). Parameters are as in Tables 1 and 2 for the Western Scheldt case and $c_h^u = 0$, $u_c = 0 \text{ m s}^{-1}$ and $n = n_{\text{pref}} = 2$. The blue curve (inertia) lies below the yellow line (diffusion). When horizontal eddy diffusivity is neglected (as in Schramkowski et al., 2002), the main balance remains between erosion and deposition for $k \approx k_{\text{pref}}$, but $n_{\text{pref}} = 3$ and k_{pref} is larger.

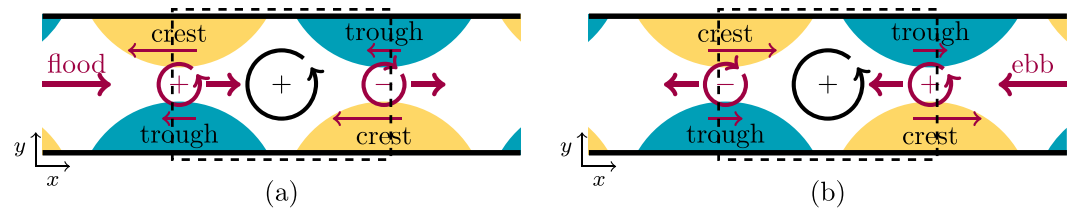


Figure 8. Generation of tidal residual vorticity cells for bottom pattern with mode number $n = 1$. (a) Situation during flood ($u_{eq} > 0$). (b) Situation during ebb ($u_{eq} < 0$). Friction (thin red arrows) experienced by water column is larger on the crests than on the troughs and generates tidal vorticity (red circles). Both during ebb and flood, positive vorticity is transported into the dashed box and the negative vorticity is transported out, resulting in the build-up of positive vorticity (black circle).

Substituting the latter in ω_{adv} shows that the contribution of the advective transport scales with the magnitude of the residual current \bar{u}_0 :

$$\omega_{adv} \approx \frac{-1}{1 - \hat{p}} \frac{\alpha k U^2}{\gamma} \bar{u}_0. \quad (15)$$

The physical mechanism can now be understood by analyzing the residual current u_0 via vorticity arguments that follow from Zimmerman (1981). For this, consider a longitudinal tidal current that moves over a bottom that consists of bars and troughs as illustrated in Figure 8 (here the $n = 1$ pattern is assumed). The lateral depth variations result in frictional torques that generate tidal vorticity, as is indicated by the red circles. This vorticity is subsequently transported by the unperturbed tidal flow. As a result, both during ebb and flood, there is an influx of vorticity of the same sign into a region between crests and troughs. Thus, residual vorticity builds up in these areas (black circles in the figure), which is balanced by dissipation due to bottom friction. The resulting residual currents turn out to be directed from the troughs to the crests in the longitudinal direction and from the crest to the troughs in the lateral direction (see also right column in Figure 3). To understand why this leads to growth of bars and deepening of troughs, consider the convergence of the tidally averaged advective sediment transport (see equations (8) and (9)). This reads, using that the equilibrium velocity u_{eq} and the equilibrium sediment concentration C_{eq} are spatially uniform,

$$-\langle C_{eq} \nabla \cdot \mathbf{u}' \rangle - \langle \mathbf{u}_{eq} \cdot \nabla C' \rangle = -\langle C_{eq} u_{eq} \rangle \frac{1}{H} \frac{\partial h'}{\partial x} - \langle u_{eq} \frac{\partial C'}{\partial x} \rangle = -\langle u_{eq} \frac{\partial C'}{\partial x} \rangle, \quad (16)$$

where for the first equality sign, the perturbed continuity equation is used and for the second one, the fact that $\langle u_{eq} C_{eq} \rangle = 0$. Equation (16) shows that convergence of sediments occurs when u_{eq} and $\partial C' / \partial x$ are negatively correlated. From equation (14), it follows that the perturbed concentration reads

$$C' \approx \frac{2\alpha}{\gamma} u_0 u_{eq}.$$

Since u_0 is directed towards the bars, this implies that both during ebb and flood, the perturbed concentration C' is positive upstream from a bar and negative downstream. On the other hand, C' is negative upstream a trough and positive downstream of it. Hence, the convergence of advective transport causes bars to grow and troughs to deepen for patterns with wavenumber k and mode number n close to the preferred ones. Figure 6 reveals that for larger k , ω_{adv} is negative. The reason is that for these patterns, the dominant balance in the concentration equation is not between erosion and deposition but that the advection term also becomes significant (Figure 7).

The second term in equation (12) is $\omega_{diff \text{ depth-int}}$. It originates from the fact that when at one location, the depth-integrated concentration C is larger than at another, a transport occurs from high to low C . Figure 6 reveals that $\omega_{diff \text{ depth-int}}$ is slightly positive for small k and negative for larger k and close to zero for wavenumbers close to the preferred wavenumber k_{pref} . That is, for patterns with large wavenumbers, the depth-integrated concentration is larger above the troughs than above the crests, while the opposite is the case for patterns with small wavenumbers. Therefore, the depth-integrated diffusive transport results in a small contribution of the growth of patterns with large wavenumbers and slightly causes decay of patterns with small wavenumbers.

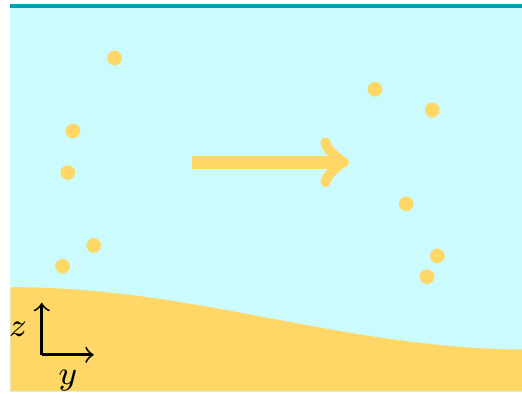


Figure 9. Consider a uniform depth-integrated concentration over a sloping bottom. On the left, the water column is shallower than on the right. Hence, the concentration $C_3(t, x, y, z)$ is larger on the left than on the right. As a result, sediments diffuse from left to right even though the depth-integrated concentrations are equal. In this case, it is the gradient in bed level that induces diffusive sediment transport instead of a gradient in depth-integrated sediment concentration.

The third term in equation (12), $\omega_{\text{diff bed slope}}$, relates to a suspended load bed slope effect. It arises in the derivation of the depth-integrated concentration equation (3) from the 3D concentration equation when the diffusion term is integrated over depth,

$$\int_{h(x)}^H \nabla \cdot (\mu \nabla C_3) dz = \nabla \cdot (\mu \nabla C) + \nabla \cdot (\mu c_b \nabla h), \quad (17)$$

where C_3 is the “3D concentration” depending on x , y and z , and c_b the concentration at the reference level above the bottom $z = h(x)$. When a balance is assumed between vertical turbulent mixing (with vertical eddy diffusivity κ_v constant over the vertical) and downward settling, the concentration at the bottom reads $c_b = (w_s/\kappa_v)\beta_b C$ (ter Brake & Schuttelaars, 2010). The first term in equation (17) results in $\omega_{\text{diff depth-int}}$ and the second in $\omega_{\text{diff bed slope}}$. The physics behind the second term becomes apparent when considering, for example, a sloping bed and a uniform depth-integrated concentration. Then, the first term, $\nabla \cdot (\mu \nabla C)$, is zero. However, in the shallow region, the concentration C_3 is higher than in the deep region, leading to sediment transport from the shallow to the deep region (Figure 9). The second term models the convergence of this transport. As the magnitude of sediment transport from crests to troughs scales with the slope, $\omega_{\text{diff bed slope}}$ is negative and becomes increasingly more negative if bottom gradients increase.

The last term of equation (12), $\omega_{\text{bl bed slope}}$, relates to bottom slope effects on bed load transport: sediment moves easier downslope than upslope. Therefore contributes $\omega_{\text{bl bed slope}}$, like the third term, to convergence of sediments in the troughs and divergence of sediments on the crests. Hence, it dampens the growth of the pattern. That is, $\omega_{\text{bl bed slope}} < 0$ and is stronger negative for larger bottom slopes. In contrast to $\omega_{\text{diff bed slope}}$ results this contribution from bed load transport processes. Figure 6 reveals that $\omega_{\text{bl bed slope}}$ is much smaller than $\omega_{\text{diff bed slope}}$, which, based on the values from Table 1, directly follows from the fact that

$$\frac{\mu w_s \beta_b \tilde{C}_{\text{eq},0} / \kappa_v}{\Lambda} \approx 5.$$

The above gives a physical argument for using a larger bed load bottom slope parameter Λ than suggested by literature (Baar et al., 2018), when a total load formula is used. It then also represents the suspended load bed slope effect when this is not explicitly taken into account.

4. Discussion

4.1. Mechanism Behind Sensitivity of Tidal Bar Wavelength to Channel Width

Here we address the third objective by discussing three important aspects of Figure 4, which shows tidal bar wavelength λ_{pref} versus channel width B .

A1. In the range of channel widths with constant n_{pref} , λ_{pref} increases with increasing B .

A2. While increasing B , the preferred wavelength λ_{pref} decreases when n_{pref} jumps to a higher mode number.

A3. The range of channel widths for which n_{pref} is the same is wider when horizontal eddy diffusivity μ in the sediment mass balance is taken into account.

Together, this shows that the wavelength depends on channel width when horizontal eddy diffusivity is taken into account and why the wavelength remains of the same order of magnitude for a large range of channel widths when the horizontal eddy diffusivity is neglected.

To analyze the three aspects above, the growth rate is first approximated as

$$\tilde{\omega} \approx \omega_{\text{adv}} + \omega_{\text{eff bed slope}}. \quad (18)$$

Here the two bed slope effects $\omega_{\text{diff bed slope}}$ and $\omega_{\text{bl bed slope}}$ are combined into an effective bed slope term

$$\omega_{\text{eff bed slope}} = \frac{-1}{1 - \hat{p}} \Lambda_{\text{eff}} (k^2 + l_n^2), \quad \text{with} \quad \Lambda_{\text{eff}} = \Lambda + \mu \frac{w_s}{\kappa_v} \beta_b \tilde{C}_{\text{eq},0}, \quad (19)$$

and $\omega_{\text{diff depth-int}}$ is neglected.

The first two aspects (A1 and A2) follow from the fact that, for a fixed mode number, the growth rate is sensitive to changes in channel width. For a fixed mode number n , the wavelength $\tilde{\lambda}$ for which $\tilde{\omega}$ is maximal is approximately (see Appendix C)

$$\tilde{\lambda}(n) = 2^{3/4} \left(\frac{\pi B}{n} \right)^{1/2} (\mathcal{L}_f^{-2} + \mathcal{L}_t^{-2})^{-1/4}, \quad (20)$$

where

$$\mathcal{L}_f = \frac{H}{8/(3\pi)c_d} \quad \text{and} \quad \mathcal{L}_t = \frac{U}{\sigma}. \quad (21)$$

Here \mathcal{L}_f is a friction length scale and \mathcal{L}_t the tidal excursion length. When $n = n_{\text{pref}}$ in equation (20), $\tilde{\lambda}(n_{\text{pref}})$ is a first-order approximation for the preferred wavelength λ_{pref} (a higher-order approximation is given in Appendix C). Equation (20) therefore yields an approximate relation between the preferred wavelength and three internal length scales of the system: the channel width B , the friction length scale \mathcal{L}_f , and the tidal excursion length \mathcal{L}_t . In its derivation, the approximate balance between erosion and deposition, see equation (14), is used and v and u_c are assumed to be zero, since including horizontal eddy viscosity ν in the momentum balance or critical erosion velocity μ was shown to be unimportant for the dependence on channel width. The first aspect (A1) is revealed by equation (20); in wider channels with the same mode number, $\tilde{\omega}$ is maximal for larger wavelengths $\tilde{\lambda}$. The second aspect (A2) also becomes apparent from equation (20). It shows that the preferred wavelength of patterns with higher mode number is smaller and hence λ_{pref} decreases when the preferred mode number n_{pref} jumps to a higher mode number.

The third aspect (A3) boils down to the statement that for a fixed channel width B , the preferred mode number n_{pref} is lower when $\mu \neq 0$ than when $\mu = 0$. This follows from a competition between the two mechanisms related to the first and second terms in equation (18). The first term increases while the second term decreases with increasing mode number n . That is, the advective term “promotes” strong lateral gradients in the bed, while the bed slope term does the opposite. As a result, if Λ_{eff} increases, n_{pref} decreases. In fact, as shown in Schramkowski et al. (2002), if $\Lambda_{\text{eff}} = 0$, the preferred mode number n_{pref} tends to infinity, but when $\Lambda_{\text{eff}} \neq 0$, the preferred mode number is finite. The essential difference between the situation where $\mu \neq 0$ compared to the case where $\mu = 0$ is that Λ_{eff} is larger in the former case and thereby a lower preferred mode n_{pref} is selected. Hence, the range of channel widths for which n_{pref} is the same is wider when horizontal eddy diffusivity μ in the sediment mass balance is taken into account.

Van der Wegen and Roelvink (2008) found a wavelength of bar patterns that, besides its dependence on current velocity and depth, scales with the square root of the channel width. In their model, the sediment transport is governed by a total load formulation (after Engelund & Hansen, 1967), where the total transport is adjusted for bed slope effects. They state that the bed slope effect is overestimated in order to obtain realistic bottom patterns. Hence, their findings correspond to the ones above, where the dependence of the wavelength to channel width is only found if the bed slope effects are relatively strong. Furthermore, equation (20) suggests that the preferred wavelength scales with the square root of channel width. Hibma et al. (2004) used a concentration equation with the bed slope effect induced by the horizontal eddy diffusivity present in their formulation. They also found tidal bar wavelength to increase with channel width.

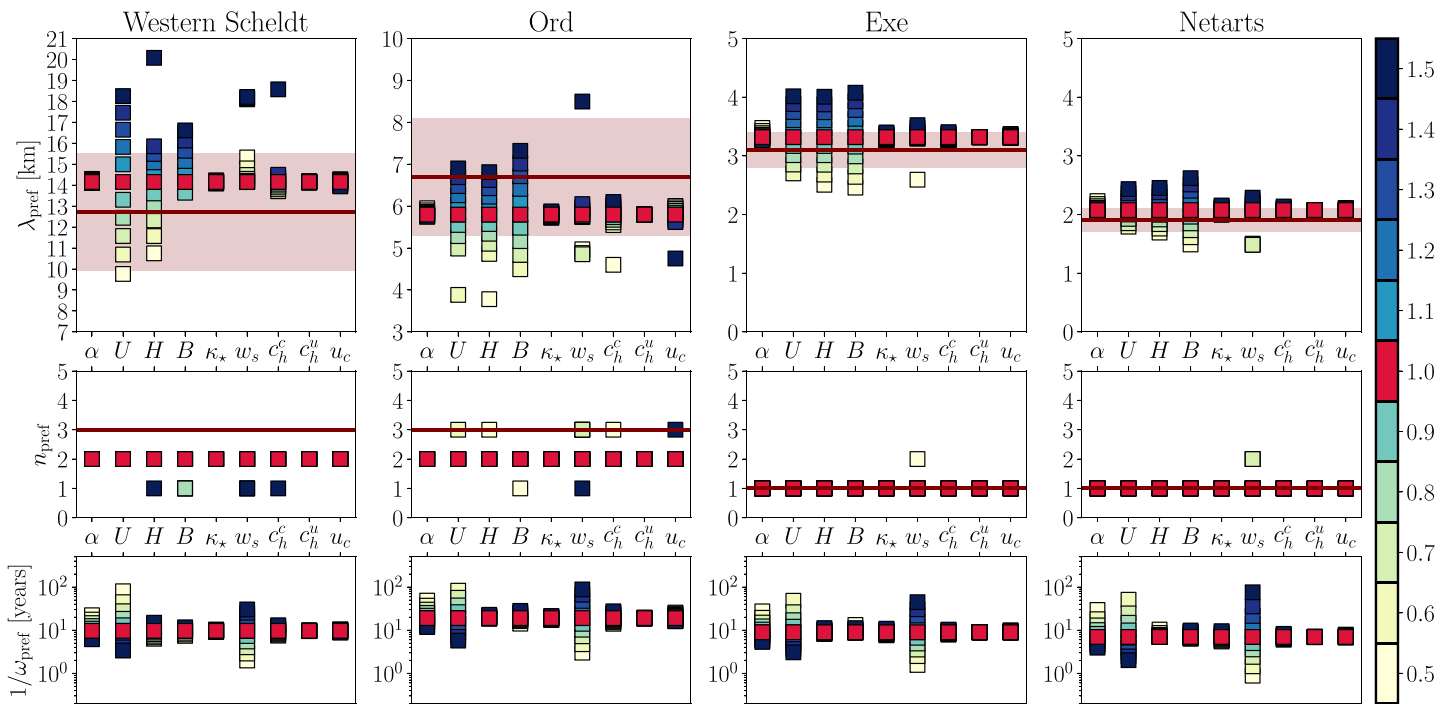


Figure 10. The preferred wavelength λ_{pref} , mode number n_{pref} , and e -folding growth time $1/\omega_{\text{pref}}$ versus different parameter values for modelled tidal bars in four different tidal channels. The colors indicate the factor with which the default parameter value is multiplied, with the red squares representing the default setting for that channel. The red lines denote the measured wavelength λ_{pref}^M and mode number n_{pref}^M as in Table 2 and the red area the measurement uncertainty (as in Figure 3). Parameter α affects the erosion, U the amplitude of the basic state tidal velocity, H the undisturbed depth, B the channel width, κ_* the bed load bed slope term, w_s the settling velocity, c_h^c the horizontal eddy diffusivity, c_h^u the horizontal eddy viscosity, and u_c the critical erosion. The parameters values are as in Tables 1 and 2 with $c_h^u = c_h^c = 0.001$ and $u_c = 0.3 \text{ m s}^{-1}$.

4.2. Sensitivity of Fluvial Bar Wavelength to River Width

Leuven et al. (2016) analyzed the fluvial bar model of Crosato and Mosselman (2009), based on Struiksmas et al. (1985). They showed that, like in the tidal bar case, the number of fluvial bars and channels in the lateral direction of the channel increases with increasing river width. Furthermore, the model of Crosato and Mosselman (2009) reveals, for a constant mode number, the increase of bar wavelength with increasing river width and also the drop in bar wavelength when the mode number increases. Moreover, when their bed slope parameter is increased, the mode number decreases. This suggests that in rivers where suspended sediment transport is significant, the horizontal eddy diffusivity will increase the sensitivity of fluvial bar wavelength to river width by the same mechanism as described above. Note there are differences: fluvial bars migrate, while tidal bars can be steady (as is the case in this study with a symmetric equilibrium current).

4.3. Sensitivity Bar Wavelength to Other Parameters

In concurrence with findings of Hibma et al. (2004), van der Wegen and Roelvink (2008), and Leuven et al. (2016), it follows from equation (20) that the preferred wavelength is, besides the channel width, sensitive to changes in current velocity and channel depth. It is therefore relevant to assess the sensitivity of the modelled λ_{pref} to these other parameters. Figure 10 shows the preferred wavelength λ_{pref} , the preferred mode number n_{pref} , and the e -folding time scale $1/\omega_{\text{pref}}$ for the four tidal channels that were introduced in section 3 (see also Figure 1). The red squares denote the results using the default parameter values for that channel (corresponding to Figure 3). In Figure 10, each default value is multiplied by factors between 0.5 and 1.5 to illustrate the sensitivity of λ_{pref} , n_{pref} , and $1/\omega_{\text{pref}}$ to these parameters. The figure reveals that, in particular for the Western Scheldt and Ord River estuary, λ_{pref} is sensitive to both current velocity U , depth H , and channel width B . In the Exe estuary and Netarts bay, the current has less influence on the preferred wavelength than in the other two channels. The jumps in λ_{pref} in the top panels correspond to jumps in mode number n_{pref} . The growth rate is most sensitive to current velocity and settling velocity.

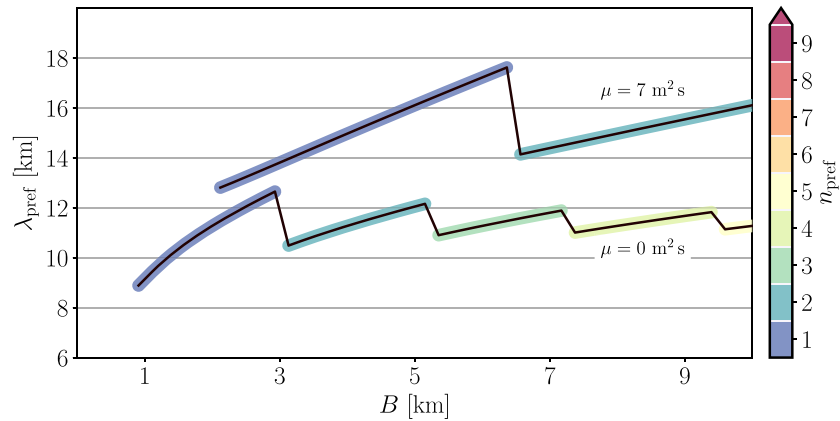


Figure 11. Preferred bar wavelength λ_{pref} versus channel width B for two values of eddy diffusivity μ (independent of channel width B). The colors denote the preferred mode number n_{pref} . Parameters are as in Tables 1 and 2 for the Western Scheldt case and $c_h^u = 0$ and $u_c = 0 \text{ m s}^{-1}$.

To further analyze the sensitivity of the preferred wavelength to the current velocity and the depth, differentiate the wavelength $\tilde{\lambda}$ with respect to the length scales B , \mathcal{L}_t , and \mathcal{L}_f to obtain, respectively,

$$\begin{aligned}\frac{\partial \tilde{\lambda}}{\partial B} &= 2^{-1/4} \sqrt{\frac{\pi}{nB}} (\mathcal{L}_t^{-2} + \mathcal{L}_f^{-2})^{-1/4}, \\ \frac{\partial \tilde{\lambda}}{\partial \mathcal{L}_t} &= 2^{-1/4} \sqrt{\frac{\pi B}{n}} \frac{1}{\mathcal{L}_t^3} (\mathcal{L}_t^{-2} + \mathcal{L}_f^{-2})^{-5/4}, \\ \frac{\partial \tilde{\lambda}}{\partial \mathcal{L}_f} &= 2^{-1/4} \sqrt{\frac{\pi B}{n}} \frac{1}{\mathcal{L}_f^3} (\mathcal{L}_t^{-2} + \mathcal{L}_f^{-2})^{-5/4}.\end{aligned}$$

The first expression approximates the slopes of the lines in the upper panels of Figure 4 for a fixed n_{pref} . It shows that when one of the length scales B , \mathcal{L}_t , and \mathcal{L}_f is very small (large), the sensitivity of $\tilde{\lambda}$ to that length scale is large (small) compared to the others. The bottom lines in the top row of Figure 4 also show this behavior; the slope of the lines decreases with increasing width B . This was also observed by Leuven et al. (2016), who found that for estuaries where the current velocity is large, the bar length hardly depends on the current velocity. Also, it agrees with the results of Dalrymple and Rhodes (1995), who found that the wavelength correlates strongly with channel width when considering channels of only a few hundred meters wide.

4.4. Formulation of Horizontal Eddy Diffusivity Coefficient

The horizontal eddy diffusivity μ is chosen to scale with the product of a velocity scale (equilibrium current velocity U) and a length scale (channel width B) such that its order of magnitude is $10 \text{ m}^2 \text{ s}^{-1}$ (Deltares, 2019). One observation from Figure 4 was that the relative change of the tidal bar wavelength over the considered range of channel widths is larger when horizontal eddy diffusivity μ was taken into account. Figure 11 reveals that is also the case when the parameterization of μ is independent of channel width B .

5. Conclusions

The model of Schramkowski et al. (2002) for tidal bars in channels is extended to include horizontal eddy diffusivity, horizontal eddy viscosity, and a critical velocity for erosion. It is shown that this model is able to mimic tidal bar patterns with length scales and growth times that are of the same order of magnitude as those of observed bars, including the sensitivity of tidal bar wavelength to channel width. In particular, the observed sensitivity of tidal bar wavelength to channel width was reproduced by taking the eddy diffusivity into account. The inclusion of horizontal eddy viscosity and critical erosion velocity did not significantly alter the relation between the tidal bar wavelength and the channel width.

The reason the extended model shows a clear dependence of tidal bar wavelength on channel width, while in the original model of Schramkowski et al. (2002) this dependence was weak, is the following. First of all, in wider channels, the pattern with the largest growth rate (the preferred tidal bar pattern) has more bars

in the lateral direction. That is, it has a higher preferred mode number. Second, in the range of channel widths with constant preferred mode number, the preferred wavelength increases with increasing channel width. However, at the width where the preferred mode number changes (it increases by one), the preferred wavelength decreases. In the model of Schramkowski et al. (2002), the range of channel widths with constant preferred mode number is relatively short. This means that, with increasing channel width, before the preferred wavelength can increase significantly, the preferred mode number increases and with that, the wavelength decreases again. As a result, the tidal bar wavelength remains of the same order of magnitude for different values of channel width. In the present study, the effects of horizontal eddy diffusivity are added to the model. As a result, the effective bed slope effect is stronger. Since bed slope effects decrease the growth rate of bottom patterns with large gradients, the bottom pattern with the largest growth rate has a smaller mode number. This implies that the preferred mode number remains the same for a wider range of channel widths than in the model of Schramkowski et al. (2002). The width dependence now follows from the fact that, in this range, the tidal bar wavelength increases with increasing channel width and that this increase is stronger for smaller mode numbers.

Appendix A : Equilibrium Pressure Gradient and Concentration

The equilibrium pressure gradient and sediment concentration are

$$(\mathbf{F}_p)_{\text{eq}} = \left(\frac{\partial \mathbf{u}_{\text{eq}}}{\partial t} + \frac{r \mathbf{u}_{\text{eq}}}{H-h}, 0 \right) \quad \text{and} \quad C_{\text{eq}} = \sum_{p=-\infty}^{\infty} \tilde{C}_{\text{eq},p} e^{ip\sigma t},$$

with

$$\tilde{C}_{\text{eq},p} = \frac{\alpha}{ip\sigma + \gamma} \left[\frac{U^2}{4} (\tilde{\mathcal{H}}_{p-2} + 2\tilde{\mathcal{H}}_p + \tilde{\mathcal{H}}_{p+2}) - \tilde{\mathcal{H}}_p u_c^2 \right].$$

In this expression

$$\mathcal{H}(\|\mathbf{u}_{\text{eq}}\|^2 - u_c^2) = \sum_{p=-\infty}^{\infty} \tilde{\mathcal{H}}_p e^{ip\sigma t},$$

with

$$\tilde{\mathcal{H}}_p = \begin{cases} \frac{i}{2\pi p} \left([e^{-ip\sigma t}]_{-\pi/\sigma}^{t_3} + [e^{-ip\sigma t}]_{t_2}^{t_1} + [e^{-ip\sigma t}]_{t_4}^{\pi/\sigma} \right) & p \neq 0, \\ \frac{\sigma}{2\pi} \left(t_3 + \frac{\pi}{\sigma} + t_1 - t_2 + \frac{\pi}{\sigma} - t_4 \right) & p = 0, \end{cases}$$

and

$$t_1 = \frac{1}{2\sigma} \cos^{-1} \left(2 \left(\frac{u_c}{U} \right)^2 - 1 \right), \quad t_2 = -t_1, \quad t_3 = t_1 - \frac{\pi}{\sigma}, \quad t_4 = -t_3.$$

Appendix B : Linearized Equations

The system of partial differential equations in the perturbed variables reads

$$H(\nabla \cdot \mathbf{u}') - \mathbf{u}_{\text{eq}} \cdot \nabla h' = 0, \quad (\text{B1})$$

$$\frac{\partial \mathbf{u}'}{\partial t} + (\mathbf{u}_{\text{eq}} \cdot \nabla) \mathbf{u}' - \nu \nabla^2 \mathbf{u}' + \mathbf{F}'_r + g \nabla \zeta' = 0, \quad (\text{B2})$$

$$\frac{\partial C'}{\partial t} + C_{\text{eq}}(\nabla \cdot \mathbf{u}') + \mathbf{u}_{\text{eq}} \cdot \nabla C' - \mu \left(\nabla^2 C' + \frac{w_s}{\kappa_v} \beta_b C_{\text{eq}} \nabla^2 h' \right) - (E' - D') = 0, \quad (\text{B3})$$

$$(1 - \hat{p}) \frac{\partial h'}{\partial t} + \nabla \cdot \langle \mathbf{q}'_s + \mathbf{q}'_b \rangle = 0, \quad (\text{B4})$$

with

$$\mathbf{F}'_r = \left(\frac{ru_{\text{eq}}h'}{H^2} + \frac{ru'}{H}, \frac{rv'}{H} \right), \quad E' = 2\alpha u_{\text{eq}} u' \mathcal{H} (\|\mathbf{u}_{\text{eq}}\|^2 - u_c), \quad D' = \gamma C',$$

and

$$\mathbf{q}'_s = \mathbf{u}' C_{\text{eq}} + \mathbf{u}_{\text{eq}} C' - \mu \left(\nabla C' + \frac{w_s}{\kappa_v} \beta_b C_{\text{eq}} \nabla h' \right) \quad \text{and} \quad \mathbf{q}'_b = -\Lambda \nabla h'.$$

The boundary conditions are

$$v' = 0, \quad \frac{\partial C'}{\partial y} = 0, \quad \frac{\partial h'}{\partial y} = 0 \quad \text{and} \quad \frac{\partial u'}{\partial y} = 0 \quad \text{at} \quad y = 0, B. \quad (\text{B5})$$

As variables u , F_p , and C are assumed bounded, this must also hold for their primed parts.

Appendix C : Approximation of Preferred Wavelength

In this appendix, we approximate the wavelength for which

$$\tilde{\omega} = \omega_{\text{adv}} + \omega_{\text{bed slope}} \quad (\text{C1})$$

is maximal for a fixed mode number n . For this, an approximate expression is derived for

$$\omega_{\text{adv}} = \frac{-1}{1 - \hat{p}} \frac{ikU}{2} (\tilde{C}_1 + \tilde{C}_{-1}).$$

Assume that $\mu = 0$ and $u_{\text{eq}} = U \cos(\sigma t)$. In the main text, it is shown that around k_{pref} , the main balance in the concentration equation is between erosion and deposition so that, with equation (14),

$$\omega_{\text{adv}} \approx \frac{-1}{1 - \hat{p}} \frac{\alpha ikU^2}{\gamma} \tilde{u}_0.$$

Next, we will approximate \tilde{u}_0 via the residual vorticity. Denote the perturbed vorticity by

$$\Omega' = \frac{\partial v'}{\partial x} - \frac{\partial u'}{\partial y} = \text{Re} \left\{ \hat{h} \sum_{p=-\infty}^{\infty} \tilde{\Omega}_p \sin(l_n y) e^{i(kx + p\sigma t)} \right\},$$

where $\tilde{\Omega}_p = ik\tilde{v}_p + l_n \tilde{u}_p$. From the tidally averaged continuity equation $\nabla \cdot \langle \mathbf{u}' \rangle = 0$, it follows that the residual velocity \tilde{u}_0 reads, in terms of the residual vorticity $\tilde{\Omega}_0$,

$$\tilde{u}_0 = \frac{l_n}{k^2 + l_n^2} \tilde{\Omega}_0. \quad (\text{C2})$$

To approximate the residual vorticity $\tilde{\Omega}_0$, consider the vorticity equation,

$$\frac{\partial \Omega'}{\partial t} + u_{\text{eq}} \frac{\partial \Omega'}{\partial x} + \frac{r}{H} \Omega' = \frac{ru_{\text{eq}}}{H^2} \frac{\partial h'}{\partial y}.$$

It shows that vorticity is advected by the current u_{eq} , dissipated by friction and generated by the flow which experiences friction and lateral depth variations. For every integer p , the Fourier coefficients $\tilde{\Omega}_p$ then satisfy

$$ip\sigma \tilde{\Omega}_p + \frac{ikU}{2} (\tilde{\Omega}_{p+1} + \tilde{\Omega}_{p-1}) + \frac{r}{H} \tilde{\Omega}_p = -\frac{rl_n}{H^2} (\tilde{u}_{\text{eq}})_p, \quad (\text{C3})$$

where $(\tilde{u}_{\text{eq}})_p$ denotes the p -th Fourier component of u_{eq} . Since $(\tilde{u}_{\text{eq}})_p \neq 0$ only for $p = \pm 1$, the lateral depth gradients only generate vorticity at the M_2 frequency. However, via the advective terms, vorticity is transported from the M_2 components to the residual component (as described in Figure 8). Neglecting the M_4 components $\Omega_{\pm 2}$, for $p = 0$ and $p = \pm 1$, equation (C3) yields

$$\tilde{\Omega}_0 = -\frac{ikUH}{2r} (\tilde{\Omega}_{-1} + \tilde{\Omega}_1) \quad \text{and} \quad \tilde{\Omega}_{\pm 1} \approx \frac{-U}{2\left(\frac{r}{H} \pm i\sigma\right)} \left(\frac{rl_n}{H^2} + ik\tilde{\Omega}_0\right).$$

Plugging the latter in the former and solving for $\tilde{\Omega}_0$ results in

$$\tilde{\Omega}_0 \approx \frac{rl_n ik}{H^2(k^2 + \tau^2)},$$

where $\tau^2 = 2(\mathcal{L}_f^{-2} + \mathcal{L}_t^{-2})$ with $\mathcal{L}_f = H/(8/(3\pi)c_d)$ and $\mathcal{L}_t = U/\sigma$. Combining this with equation (C2) results in

$$\tilde{u}_0 \approx \frac{rl_n^2 ik}{H^2(k^2 + l_n^2)(k^2 + \tau^2)}. \quad (\text{C4})$$

Hence,

$$\omega_{\text{adv}} \approx \frac{-1}{1 - \hat{p}} \frac{\alpha ik U^2}{\gamma} \tilde{u}_0 \approx \frac{\alpha U^2 k^2 l_n^2 r}{(1 - \hat{p})\gamma H^2 (k^2 + l_n^2)(k^2 + \tau^2)}. \quad (\text{C5})$$

Plugging this in equation (C1) together with the expression for $\omega_{\text{bed slope}}$ in equation (19) yields

$$\tilde{\omega} \approx a \frac{k^2 l_n^2}{(k^2 + l_n^2)(k^2 + \tau^2)} - \Lambda_{\text{eff}}(k^2 + l_n^2), \quad (\text{C6})$$

where

$$a = \frac{\alpha U^2 r}{(1 - \hat{p})\gamma H^2} \quad \text{and} \quad \Lambda_{\text{eff}} = \Lambda + \mu \frac{w_s}{\kappa_v} \beta_b \tilde{C}_{\text{eq},0}.$$

To asymptotically approximate the wavenumber for which $\tilde{\omega}$ is maximal, scale k , l_n , and τ with the tidal excursion length \mathcal{L}_t ,

$$k^* = k\mathcal{L}_t, \quad l_n^* = l_n\mathcal{L}_t \quad \text{and} \quad \tau^* = \tau\mathcal{L}_t.$$

Substituting these in equation (C6) and divide by a results in

$$\omega^* \approx \frac{k^{*2} l_n^{*2}}{(k^{*2} + l_n^{*2})(k^{*2} + \tau^{*2})} - \varepsilon(k^{*2} + l_n^{*2}), \quad (\text{C7})$$

where $\omega^* = \tilde{\omega}/a$ and $\varepsilon = \Lambda_{\text{eff}}/(a\mathcal{L}_t^2)$, which is much smaller than one. To find the k^* for which ω^* is maximal, differentiate ω^* with respect to k^* and equate with zero to obtain

$$l_n^{*2} (l_n^{*2} \tau^{*2} - k^{*4}) - \varepsilon (k^{*2} + l_n^{*2})^2 (k^{*2} + \tau^{*2})^2 = 0. \quad (\text{C8})$$

Here we divided by $2k^*$, thereby excluding the pattern that is uniform in the longitudinal direction ($k^* = 0$), since ω^* obtains a local minimum there. Plugging the asymptotic expansion $k^* = k_0^* + \varepsilon k_1^* + O(\varepsilon^2)$ in equation (C8) and equate terms of $O(1)$ yields $l_n^{*2} ((l_n^{*2} \tau^{*2})^2 - k_0^{*4}) = 0$. Therefore, looking only for real and positive wavenumbers,

$$k_0^* = \sqrt{l_n^{*2} \tau^{*2}}.$$

The corresponding dimensional wavelength $\tilde{\lambda} = \mathcal{L}_t 2\pi/k_0^*$ reads

$$\tilde{\lambda} = \frac{2\pi}{\sqrt{l_n \tau}} = 2^{3/4} \left(\frac{\pi B}{n}\right)^{1/2} (\mathcal{L}_f^{-2} + \mathcal{L}_t^{-2})^{-1/4},$$

which is the same as equation (20) in the main text. For a higher-order approximation, equate the $O(\varepsilon)$ terms of equation (C8) to obtain

$$2(l_n^* k_1^* k_0^*)^2 + (k_0^* + l_n^{*2})(k_0^* + \tau^*)^2 = 0$$

and hence,

$$k_1^* = -(l_n^* + \tau^*)^2 \sqrt{\frac{\tau^*}{4l_n^*}}.$$

Thus, the wavelength $\lambda^* = 2\pi/k^*$ for which ω^* is maximal is

$$\lambda^* = \frac{2\pi}{k_0^* + \varepsilon k_1^* + O(\varepsilon^2)} = \frac{2\pi}{k_0^*} \left(1 - \varepsilon \frac{k_1^*}{k_0^*} + O(\varepsilon^2) \right),$$

which reads in dimensional form

$$\mathcal{L}_t \lambda^* = \frac{2\pi}{\sqrt{l_n} \tau} + \frac{\Lambda_{\text{eff}} (l_n + \tau)^2}{a 2l_n}.$$

Acknowledgments

The data from the Google Earth images is included in Figure 1 and Table 2. The model is described in section 2. We thank George Schramkowski and Jelle Soons for their valuable comments and discussions.

References

- Baar, A. W., de Smit, J., Uijttewaai, W. S. J., & Kleinhans, M. G. (2018). Sediment transport of fine sand to fine gravel on transverse bed slopes in rotating annular flume experiments. *Water Resources Research*, *54*, 19–45. <https://doi.org/10.1002/2017WR020604>
- Bailard, J. A. (1981). An energetics total load sediment transport model for a plane sloping beach. *Journal of Geophysical Research*, *86*(C11), 10,938–10,954. <https://doi.org/10.1029/JC086iC11p10938>
- Cancino, L., & Neves, R. (1999). Hydrodynamic and sediment suspension modelling in estuarine systems: Part II: Application to the Western Scheldt and Gironde estuaries. *Journal of Marine Systems*, *22*(2), 117–131. [https://doi.org/10.1016/S0924-7963\(99\)00036-6](https://doi.org/10.1016/S0924-7963(99)00036-6)
- Crosato, A., & Mosselman, E. (2009). Simple physics-based predictor for the number of river bars and the transition between meandering and braiding. *Water Resources Research*, *45*, W03424. <https://doi.org/10.1029/2008WR007242>
- Dalrymple, R. W., & Rhodes, R. M. (1995). Estuarine dunes and bars. In G. M. E. Perillo (Ed.), *Geomorphology and sedimentology of estuaries. Developments in sedimentology* (pp. 359–422). Amsterdam: Elsevier Science B.V.
- Deltares (2019). *User manual Delft3d-Flow: Simulation of multi-dimensional hydrodynamic flows and transport phenomena, including sediments (version 3.15)*. Boussinesqweg 1, 2629 HV Delft, The Netherlands: Deltares.
- Dodd, N., Blondeaux, P., Calvete, D., de Swart, H. E., Falqués, A., Hulscher, S. J. M. H., et al. (2003). Understanding coastal morphodynamics using stability methods. *Journal of Coastal Research*, *19*(4), 849–865. <https://www.jstor.org/stable/4299224>
- Dyer, K. R. (1986). *Coastal and estuarine sediment dynamics*. Chichester: John Wiley & Sons.
- Engelund, F., & Hansen, E. (1967). A monograph on sediment transport in alluvial streams. Copenhagen, Denmark: Teknisk Forlag.
- Garotta, V., Bolla Pittaluga, M., & Seminara, G. (2006). On the migration of tidal free bars. *Physics of Fluids*, *18*(9), 96601. <https://doi.org/10.1063/1.2221346>
- Glanzmann, C. F., Blenne, B., & Burgess, F. J. (1971). Tidal hydraulics, flushing characteristics and water quality of Netarts bay (*Tech. Rep.*) Corvallis, Oregon: Engineering Experiment Station, Oregon State University.
- Herrmann, R., & Hübner, D. (1982). Behaviour of polycyclic aromatic hydrocarbons in the Exe estuary, Devon. *Netherlands Journal of Sea Research*, *15*(3), 362–390. [https://doi.org/10.1016/0077-7579\(82\)90065-5](https://doi.org/10.1016/0077-7579(82)90065-5)
- Hibma, A., Schuttelaars, H. M., & de Vriend, H. J. (2004). Initial formation and long-term evolution of channel-shoal patterns. *Continental Shelf Research*, *24*, 1637–1650. <https://doi.org/10.1016/j.csr.2004.05.003>
- Krol, M. (1991). On the averaging method in nearly time-periodic advection-diffusion problems. *SIAM Journal on Applied Mathematics*, *51*(6), 1622–1637. <https://doi.org/10.1137/0151083>
- Leuven, J. R. F. W., Kleinhans, M. G., Weisscher, S. A. H., & van der Vegt, M. (2016). Tidal sand bar dimensions and shapes in estuaries. *Earth-Science Reviews*, *161*, 204–223. <https://doi.org/10.1016/j.earscirev.2016.08.004>
- Press, W. H., Teukolsky, S. A., Vetterling, W. T., & Flannery, B. P. (2007). *Numerical recipes: The art of scientific computing* (3rd ed.). New York: Cambridge University Press.
- Schramkowski, G. P., Schuttelaars, H. M., & de Swart, H. E. (2002). The effect of geometry and bottom friction on local bed forms in a tidal embayment. *Continental Shelf Research*, *22*(11), 1821–1833. (Proceedings from the Tenth Biennial Conference on the Physics of Estuaries and Coastal Seas) [https://doi.org/10.1016/S0278-4343\(02\)00040-7](https://doi.org/10.1016/S0278-4343(02)00040-7)
- Schuttelaars, H. M., & de Swart, H. E. (1999). Initial formation of channels and shoals in a short tidal embayment. *Journal of Fluid Mechanics*, *386*, 15–42. <https://doi.org/10.1017/S0022112099004395>
- Seminara, G., & Tubino, M. (2001). Sand bars in tidal channels. Part 1. Free bars. *Journal of Fluid Mechanics*, *440*, 49–74. <https://doi.org/10.1017/S0022112001004748>
- Smith, J. D., & McLean, S. R. (1977). Spatially averaged flow over a wavy surface. *Journal of Geophysical Research*, *82*(12), 1735–1746. <https://doi.org/10.1029/JC082i012p01735>
- Soulsby, R. (1997). *Dynamics of marine sands*. London: Thomas Telford.
- Struikma, N., Olesen, K. W., Flokstra, C., & de Vriend, H. J. (1985). Bed deformation in curved alluvial channels. *Journal of Hydraulic Research*, *23*(1), 57–79. <https://doi.org/10.1080/00221688509499377>
- Tamboni, N., Pittaluga, M. B., & Seminara, G. (2005). Laboratory observations of the morphodynamic evolution of tidal channels and tidal inlets. *Journal of Geophysical Research*, *110*, F04009. <https://doi.org/10.1029/2004JF000243>

- ter Brake, M. C., & Schuttelaars, H. M. (2010). Modeling equilibrium bed profiles of short tidal embayments. *Ocean Dynamics*, *60*(2), 183–204. <https://doi.org/10.1007/s10236-009-0232-3>
- ter Brake, M. C., & Schuttelaars, H. M. (2011). Channel and shoal development in a short tidal embayment: An idealized model study. *Journal of Fluid Mechanics*, *667*, 503–529. <https://doi.org/10.1017/jfm.2011.97>
- van de Lageweg, W. I., & Feldman, H. (2018). Process-based modelling of morphodynamics and bar architecture in confined basins with fluvial and tidal currents. *Marine Geology*, *398*, 35–47. <https://doi.org/10.1016/j.margeo.2018.01.002>
- van der Wegen, M., & Roelvink, J. A. (2008). Long-term morphodynamic evolution of a tidal embayment using a two-dimensional, process-based model. *Journal of Geophysical Research*, *113*, C03016. <https://doi.org/10.1029/2006JC003983>
- Wolanski, E., Moore, K., Spagnol, S., D'Adamo, N., & Pattiaratchi, C. (2001). Rapid, human-induced siltation of the macro-tidal Ord River estuary, Western Australia. *Estuarine, Coastal and Shelf Science*, *53*(5), 717–732. <https://doi.org/10.1006/ecss.2001.0799>
- Zimmerman, J. T. F. (1981). Dynamics, diffusion and geomorphological significance of tidal residual eddies. *Nature*, *290*, 549–555. <https://doi.org/10.1038/290549a0>

Erratum

The originally published version of this manuscript contained typesetting errors in equations (8), (9), (13), (B4), and in the equation immediately below equation (B4). Additionally, numerous vectors were not typeset in bold font, making them indistinguishable from scalars with the same name. These errors, along with other minor typographical errors introduced during typesetting, have been corrected, and this may be considered the official version of record.